EuBaFe$_2$O$_5$: Extent of charge ordering by Mössbauer spectroscopy and high-intensity high-resolution powder diffraction

P. Karen[a,*], K. Gustafsson[b], J. Lindén[b]

[a]*Department of Chemistry, University of Oslo, P.O. Box 1033 Blindern, N-0315 Oslo, Norway*
[b]*Department of Physics, Åbo Akademi, FI-20500 Turku, Finland*

Abstract

[151]Eu and [57]Fe Mössbauer spectroscopy, differential scanning calorimetry, and high-intensity high-resolution synchrotron powder diffraction were used to determine the extent of long- and short-range charge ordering below the first-order Verwey-type transition in EuBaFe$_2$O$_5$, the oxygen content of which was homogenized by annealing in sealed ampoule. The diffraction gives 0.68(5) valence unit of charge separation at 100 K. Interpretation of this value as 68% of iron being long-range charge ordered correlates with the total transition entropy per formula of about 0.7 of the theoretical value $2R \ln 2$ that would be valid for all iron atoms being fully charge ordered. For long- and short-range order combined, [57]Fe Mössbauer spectroscopy suggests that about 90% of iron atoms occur as charge-ordered integer Fe^{2+} and Fe^{3+}. The residual 10% are the Fe^{2+} and Fe^{3+} that did not find the way to order. Local oxygen non-stoichiometry defects that revert the direction of the charge order are suggested as one of the origins of the short-range charge order. Accordingly, the long-range charge order seen by diffraction is highest in the portion of the sample that converts last upon heating, having the most ideal valence ratio.
© 2006 Elsevier Inc. All rights reserved.

PACS: 61.10.Nz; 61.18.Fs; 61.50.Ks; 82.60.Fa

Keywords: Charge ordering; Mixed valence; Iron perovoskite oxides; Verwey transition; [151]Eu and [57]Fe Mössbauer spectroscopy

1. Introduction

Interest in charge ordering and valence mixing in iron oxides stems from the archetype of such phases, magnetite, Fe$_3$O$_4$. As a double-exchange ferromagnet, Fe$_3$O$_4$ has potential applications related to spin-polarized conduction above the Verwey transition [1]. At ~120 K magnetite becomes a source of spin-polarized carriers; viz., electrons associated with the thermal valence mixing. However, below this transition temperature, the situation is complex and results from various methods do not agree. Separation of the octahedral spinel sites towards unequal di- and trivalent iron is suggested by synchrotron X-ray and neutron diffraction of high-quality powder samples [2], by resonant X-ray diffraction at the Fe absorption edge [3,4], and is followed by

quantum-chemical calculations [5,6]. Alternatively, [57]Fe Mössbauer data have recently been interpreted [7,8] as an indicative of a switch to a direct-spinel type below Verwey transition where divalent iron enters the tetrahedral sites originally occupied by trivalent iron. Because the low-temperature crystal structure of magnetite is complex and the eventual charge separation weak [2], the evidence is mixed. Methods such as EXAFS [9] and [57]Fe NMR [10] suggest no ordering or are inconclusive, high-energy resonant soft X-ray photoemission [11] and single-crystal Mössbauer spectroscopy [12] speak in favor of it. Some authors [8,13,14] therefore conclude that charge separation and ordering is not what occurs below the Verwey transition in magnetite, or, for that matter, in similar cases of transition metal oxides [15]. The problem is made worse by the high sensitivity of the Verwey transition to non-stoichiometry in magnetite [16,17], which makes it difficult to obtain good quality samples and apply methods of low penetration depth.

---

*Corresponding author. Fax: +47 228 554 41.

E-mail address: pavel.karen@kjemi.uio.no (P. Karen).

The term Verwey transition has traditionally been used also for similar first-order transitions, such as in YFe_2O_4 [18], $LiMn_2O_4$ [19], Eu_3O_4 [20] and EuNiP [21]. The recently synthesized [22] $RBaFe_2O_5$ (R = rare-earth atom) is the hitherto only such phase of the non-tilted perovskite type. It exhibits all symptoms of the Verwey transition: conductivity change by two orders of magnitude [23,24], thermal effect [25,26], change in unit-cell volume and deformation [25], first-order transition [25]. The same features are shown by high-quality Fe_3O_4: conductivity [27], thermal effect [16], volume change [28], first-order transition [29]. The only difference is that at subambient temperatures the double exchange in magnetite makes it a better conductor, although still polaronic [27,30].

In $RBaFe_2O_5$ at high temperatures, valence-mixed $Fe^{2.5+}$ state is formed [31] whereas, at low temperatures, Mössbauer spectroscopy [25,31], synchrotron X-ray powder diffraction (SXPD) [23,25,26,32] and neutron powder diffraction (NPD) [23,25,33,34] reveal signs of a two-step charge separation and ordering. The first step is weaker and in several aspects premonitory to what happens at the second step. At T_p = 285–335 K, depending on R [26], incipient states $Fe^{2.5+\varepsilon}$ and $Fe^{2.5-\varepsilon}$ are discerned by ^{57}Fe-Mössbauer spectroscopy [25]. This disproportionation is facilitated by the small orthorhombic distortion that is present in the structure below the Néel temperature T_N = 420 K [34]. No powder diffraction technique is able to detect any long-range order for this partial charge separation [23,33,34]. At a somewhat lower temperature T_V = 210–310 K, depending on R [26], the second charge-ordering step has the major symptoms of the first-order Verwey transition. Superstructure reflections appearing in the powder diffraction patterns suggest ordering of oxygens around two non-equivalent iron sites. The actual charge-ordering arrangement [25] does not correspond to coulombic minimization of point charges, implying ordering of spatial charges, orbitals [33].

From the recent review [35] it follows that among phases that undergo charge ordering at low temperatures, the long-range charge separation of the two different Fe atomic environments, as seen by powder diffraction, is rarely larger than about half a valence unit. The extent of the charge separation is also clearly correlating with the degree of the associated sterical frustration. Owing to the ordering of the R and Ba atoms, as well as O vacancies, the double-cell perovskite structure of $RBaFe_2O_5$ maintains high symmetry, and the iron–oxygen coordination polyhedra are not tilted. Providing arguably least frustration for ordering of iron charges (valences), orbitals and spins, the title phase is ideal for maximum charge separation. The extent of the long-range charge ordering below and across the Verwey transition is investigated in the present study with high-resolution, high-intensity SXPD on an $EuBaFe_2O_{5.004}$ sample of high oxygen homogeneity achieved by prolonged annealing. The long- and short-range ordered valence and spin states of iron are accounted for by ^{57}Fe-Mössbauer spectroscopy. These data are complemented by ^{151}Eu-

Mössbauer spectroscopy as a probe into the local atomic and magnetic environments of the rare-earth atom.

2. Experimental

Syntheses: The master sample of $EuBaFe_2O_{5+w}$ was synthesized from amorphous precursors obtained by liquid mixing in melted citric acid. Standardized Eu_2O_3 (99.99%, Molycorp) was dry-mixed with 40 times its molar amount of high-purity citric acid monohydrate (Fluka, <0.02% sulphate ash) and dissolved upon melting assisted by a small amount of water. Iron (lumps, 99.95%, Koch-Light) was dissolved in dilute HNO_3 and gradually added into the melt while the mixture was warmed up until nitrose gases ceased to develop. After cooling below 100 °C, re-distilled water was added and barium carbonate (Fluka, <0.2% Sr) was dissolved. Resulting clear viscous melt was decomposed into an organic-based solid at 200 °C, homogenized in a vibration mill and incinerated for 5 days in a covered porcelain crucible at 390 °C. The obtained X-ray amorphous powder was calcined for 20 h at 900 °C, milled, pressed (150 bar) into cylinders and sintered on a powder bed of the same composition at 1000 °C in wet mixtures of argon and hydrogen (Table 1). The single-phase product (according to SXPD) was completely sintered.

Oxygen content control: $EuBaFe_2O_{5.001}$ was obtained by equilibration for 7 days in an Ar–H_2–H_2O atmosphere of a high-purity premixed gas (Ar/H_2 = 8.82 by volume) having $\log_{10}(p_{H_2O}/bar)$ = −4.35 (measured by an Endress–Hauser hygrometer) and $\log_{10}(p_{O_2}/bar)$ = −27.07 at temperature 640 °C, from which the sample was quenched. An $EuBaFe_2O_{5.010}$ sample for Mössbauer experiments and several similar compositions were obtained analogously. After subsequent homogenization of $EuBaFe_2O_{5.001}$ for 10 days at 500 °C in a sealed evacuated quartz ampoule with a small amount of Zr getter heated locally to 800 °C, followed by slow cooling overnight, the oxygen content according to cerimetric titration [22] was w = 0.004.

SXPD: Data for the refinement of the charge-ordered superstructure at 100 K were collected with wavelength λ = 0.40003 Å on the high-intensity, high-resolution ID31 diffractometer at the ESRF Grenoble in steps of 0.0005° 2θ over a redundant angular range to ensure good contribution from all 9 parallel detectors. Data collection between −6° and 30° 2θ at the detector 1 took 3 h, between 30° and 45° 2.5 h. The raw data were averaged into steps of 0.0015° 2θ. The powder sample was sealed in a glass

Table 1
Synthesis conditions (temperature t in °C, pressure p in bars) of the $EuBaFe_2O_{5+w}$ master sample

	t	Ar/H_2[a]	$\log_{10}(p_{H_2O})$	$\log_{10}(p_{O_2})$
Calcination	900	121(3)	−1.65(1)	−15.25(4)
Sintering	1000	16.5(2)	−1.65(1)	−15.24(1)

[a]By volume; standard deviations refer to variations over time.

capillary of 0.35 mm in diameter and rotated at $60 \, s^{-1}$ in the beam of a 1.5×2 mm area. Temperature was controlled by a nitrogen gas flow from a 700 series Oxford Cryostream Plus. Short isothermal scans across the temperature range of the Verwey transition were performed between $2°$ and $26°$, step size $0.002°$ in 2θ. Rietveld refinements were done with the GSAS software suite [36]. Strain anisotropy coefficients S_{hkl} of Stephens [37] were used to model the asymmetry of Bragg peaks caused by the distribution of the oxygen non-stoichiometry [32] across the sample. CIF files can be obtained from the Fachinformationszentrum Karlsruhe, 76344 Eggenstein-Leopoldshafen, Germany, fax: (49)7247-808-666, e-mail: crysdata@fiz-karlsruhe.de, on quoting the depository number CSD 416716 for $EuBaFe_2O_5$ at 100 K and CSD 416717 at 300 K.

Bond-valence calculations: For calculations of the bond-valence sums (BVS) bond-valence parameters by Brown were used [38]: $R_0 = 2.074$ Å for Eu, 2.285 Å for Ba, 1.734 Å (Fe^{2+}) for the "larger" iron atom Fe(2), and 1.759 Å (Fe^{3+}) for the "smaller" iron atom Fe(1). Above Verwey transition, $R_0 = 1.7466$ was used for the valence-mixed iron.

Differential scanning calorimetry (*DSC*): A liquid-nitrogen operated Perkin–Elmer Pyris 1 instrument was used to register thermal flux curves upon heating (10 K/min) between 170 and 340 K. A more detailed description is in Ref. [32].

Mössbauer spectroscopy: Absorbers were made by homogenizing $\sim$70 mg of the powdered sample with epoxy resin across a 20 mm diameter circle on an Al foil. ^{57}Fe spectra were recorded at constant temperatures between 77 and 323 K, in transmission geometry, with a fresh Cyclotron ^{57}Co:Rh (25 mCi) source. ^{151}Eu spectra were collected between 243 and 318 K for two to four weeks each, with a ^{151}Sm:Sm_2O_3 (100 mCi) source of the

production year 1968. The ^{57}Fe and ^{151}Eu spectra were measured on the same transducer using the maximum Doppler velocity of 11.15 mm/s. For the ^{57}Fe measurements, temperatures were maintained with an accuracy of ± 0.3 K with an Oxford ITC5 continuous-flow cryostat. All ^{151}Eu measurements were done using a dedicated Peltier cooling/heating device, with stability better than ± 0.03 K. The Peltier cooling device was also used for the ^{57}Fe spectra recorded at temperatures around T_V and T_p. The ^{57}Fe spectra were fitted with full Hamiltonian of combined electric and magnetic interactions and following parameters: internal magnetic field at the nucleus (B) and its Gaussian distribution width (ΔB), the chemical isomer shift relative to α-Fe at 300 K (δ), the quadrupole coupling constant (eQV_{zz}), the resonance line widths (Γ), the asymmetry parameter η, the angles α and β specifying the direction of the internal field versus the electric field gradient, and the relative intensities of the spectral components of various Fe species (I). All identified components were constrained to have equal line widths Γ. The ^{151}Eu spectra were fitted with one single Mössbauer component of combined electric and magnetic interactions with analogous parameters as above (except ΔB and I).

3. Results

3.1. Structural data

3.1.1. The crystal structure of charge-ordered EuBaFe$_2$O$_5$

Fifty four Bragg peaks belonging to the *a*-doubled superstructure of the parent double-cell perovskite were identified by visual inspection of the diffraction pattern of the charge-ordered $EuBaFe_2O_{5.004}$ phase at 100 K. Eleven of them are shown in the inset of Fig. 1. The very good

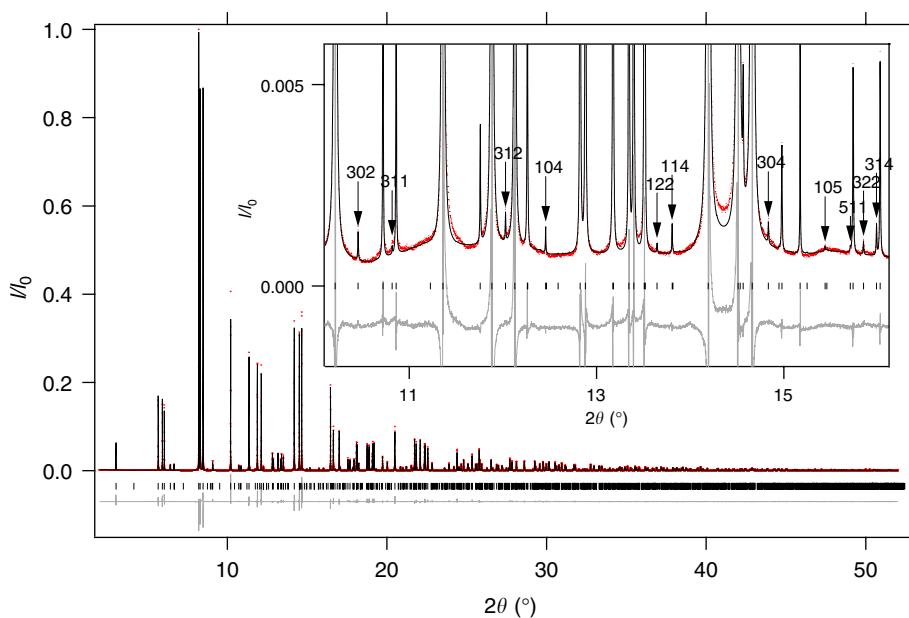Fig. 1. Rietveld refinement of charge-ordered EuBaFe$_2$O$_{5.004}$ (100 K, ID31 diffractometer, $\lambda = 0.40003$ Å). The inset shows a slice with 11 of the 54 discerned superstructure Bragg reflections (marked with *hkl* labels).

background-to-peak resolution makes it possible to reliably refine the shifts of oxygen atoms towards the iron that is becoming trivalent under charge ordering. The refined structure parameters are listed in Table 2.

The oxygen-homogenization procedure clearly reduced the asymmetry of the Bragg peaks of the charge-ordered phase. Their shape is better than for the $R = $ Gd case [32] (not annealed; modelled by 8 profiles) and $R = $ Dy [26] (annealed, modelled by 2 profiles). The remaining asymmetry in the present sample is in part taken care of by refining the anisotropic strain. However, a residual misfit is still apparent from the asymmetric difference curves and increased background between peaks that were split by the orthorhombic distortion (Fig. 1), and it is the cause for the relatively large R_{wp} and R_p figures of merit in Table 2.

The bond distances in the two unequal iron-coordination square pyramids (Fig. 2) are close to those obtained by structure refinements from the NPD data on $TbBaFe_2O_{5.012}$ [25]. The same is valid for standard deviations, suggesting that high-intensity SXPD is now able to see the light oxygen atoms in oxides like this one with as much resolution as NPD. The magnitude of the charge separation between the two iron atoms in the long-range charge-ordered sample does not follow directly from SXPD. The commonly adopted approach is to use bond-valence parameters and calculate BVS for the two unequal iron atoms. Fig. 2 shows that their bond distances are different far beyond standard deviations. Table 3 lists bond distances and calculated BVS for all atoms in the unit cell at 100 K. Considering that the R_0 parameters refer to room temperature, the low-temperature contraction adds certain small false overbonding to all atoms. From data in Table 3

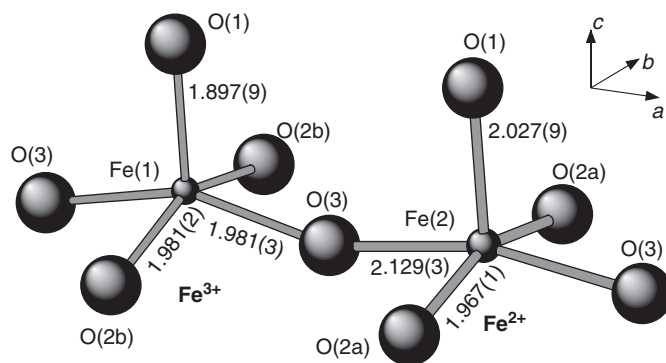Fig. 2. Environments of the two crystallographically different Fe atoms in charge-ordered $EuBaFe_2O_5$ at 100 K as refined from SXPD data; distances in Å.

Table 3
Bond distances (in Å) and bond valence sums (BVS) calculated from refined structural parameters for charge-ordered $EuBaFe_2O_{5.004}$ at 100 K

Atom	Eu	Ba	Fe(1)	Fe(2)	BVS
O(1)		$4 \times 2.7963(1)$	$1 \times 1.897(9)$	$1 \times 2.027(9)$	2.145(27)
O(2a)	$2 \times 2.457(6)$	$2 \times 3.130(5)$		$2 \times 1.967(1)$	1.975(13)
O(2b)	$2 \times 2.482(4)$	$2 \times 3.096(5)$	$2 \times 1.981(2)$		1.985(14)
O(3)	$4 \times 2.422(1)$	$4 \times 3.027(1)$	$2 \times 1.981(3)$	$2 \times 2.129(3)$	1.941(11)
BVS	2.934(17)	1.969(8)	2.883(31)	2.201(21)	

it follows that the average valence separation (degree of charge ordering) of the two non-equivalent iron atoms is 0.68(5).

3.1.2. Structural evolution of $EuBaFe_2O_5$ across the Verwey transition

Many of the weak Bragg reflections of the charge-ordered superstructure are apparent also on the short isothermal scans collected at several temperatures upon heating through the Verwey transition. Fig. 3 illustrates such an evolution on a group of very weak double-perovskite-type reflections so that comparison with one of the strongest superstructure Bragg lines (102) can be made. It is seen that the charge-ordered phase with a large orthorhombic distortion is gradually disappearing in favor of the valence-mixed phase, and that this happens within a relatively narrow interval of this first-order transition.

These short scans were used in Rietveld refinements to obtain atomic coordinates for the charge-ordered phase. The result in Fig. 4 shows a remarkable change right before the Verwey transition upon heating. The essence of this change is that the divalent iron atom is moving towards the base of the coordination square pyramid, whereas the trivalent iron moves towards its center of gravity. For interpretation of any such change it is important to keep in mind that non-stoichiometric oxides have a small distribution of their oxygen content across the bulk [32]. Because T_V decreases with increasing w in $EuBaFe_2O_{5+w}$, the most

Table 2
Charge-ordered $EuBaFe_2O_{5.004}$ at 100 K; SXPD structure refinement

Unit cell		Refinement statistics	
Space group	*Pmma*	R_{wp}	0.0891
a (Å)	8.084222(5)	R_p	0.0641
b (Å)	3.864880(2)	$R(F^2)$	0.0383
c (Å)	7.574368(4)	N_{obs}	1514
V (Å³)	236.658(0)	N_{vars}	23

Atom	Site	n	x	y	z	U_{iso} [a]
Eu	2c	1	0	0	$\frac{1}{2}$	0.00174(5)
Ba	2a	1	0	0	0	0.00297(7)
Fe(1)	2f	1	$\frac{1}{4}$	$\frac{1}{2}$	0.25226(15)	0.00233(6)
Fe(2)	2f	1	$\frac{3}{4}$	$\frac{1}{2}$	0.26589(13)	0.00233(6)
O(1)	2f	1	$\frac{1}{4}$	$\frac{1}{2}$	0.0018(10)	0.0032(2)
O(2a)	2e	1	$\frac{3}{4}$	0	0.3156(8)	0.0032(2)
O(2b)	2e	1	$\frac{1}{4}$	0	0.3097(8)	0.0032(2)
O(3)	4j	1	0.0104(5)	$\frac{1}{2}$	0.3075(2)	0.0032(2)
O(4)	2f	0.004	$\frac{1}{4}$	$\frac{1}{2}$	$\frac{1}{2}$	0.0032(2)

[a] In Å²; constrained equal for both irons and for all oxygens.
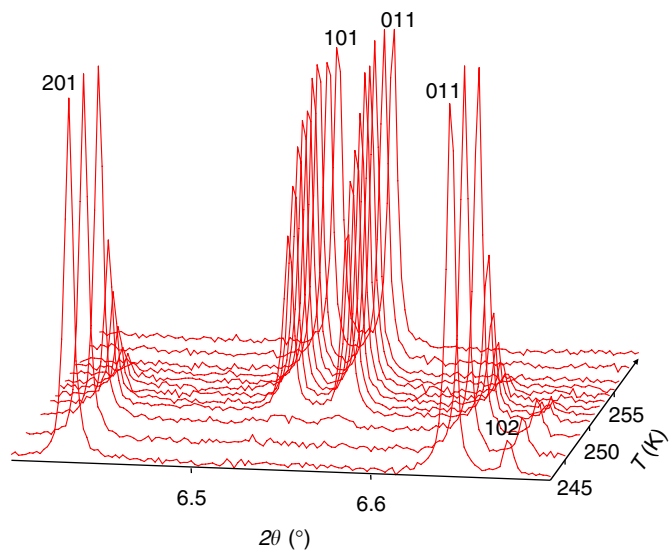
Fig. 3. Sections of raw ID31 data for $EuBaFe_2O_{5.004}$ upon warming through the Verwey transition. Note the vanishing superstructure Bragg reflection 1 0 2.

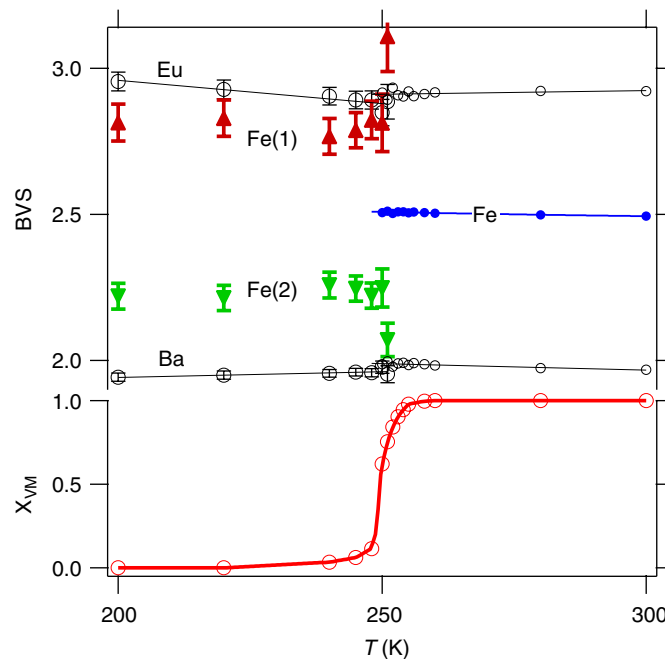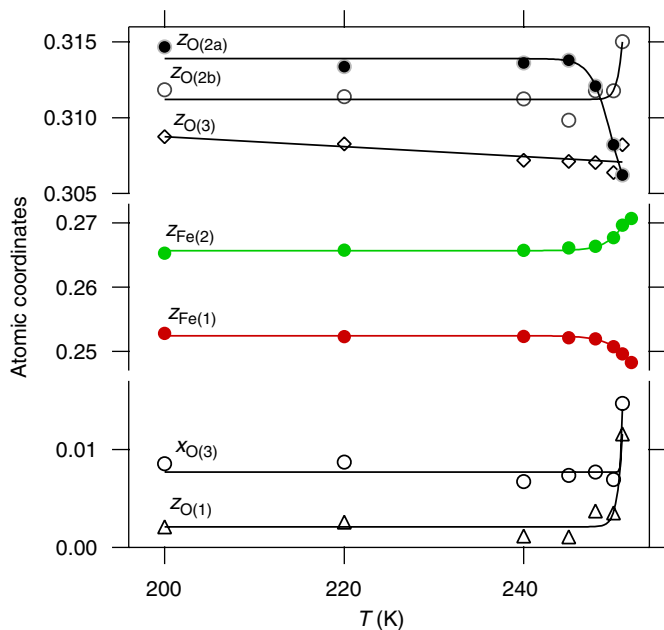Fig. 4. Thermal evolution of atomic coordinates for charge-ordered $EuBaFe_2O_{5.004}$. At 252 K, only iron coordinates were refinable.

Fig. 5. $EuBaFe_2O_{5.004}$: evolution across the Verwey transition of bond-valence sums (BVS) and molar fractions for the valence-mixed phase (x_{VM}). Size of the symbols in the valence-mixed region is larger than standard deviations.

3.2. DSC

The transition temperatures for precisely stoichiometric $EuBaFe_2O_5$ were estimated from data for several samples within oxygen non-stoichiometry of ±0.010. The premonitory charge-ordering temperature is $T_p = 299(4)$ K, the main charge-ordering temperature is $T_V = 256.3(4)$ K. Furthermore, DSC registers the latent heat associated with the discontinuous charge freezing in $EuBaFe_2O_5$ against the volume work. The corresponding entropy total for the premonitory and main Verwey transitions is 8.2(1) J/(mol K) per ideal formula $EuBaFe_2O_5$. This entropy is about 0.7 of the theoretical value of $2R\ln 2$, hence close to the degree of the coherent long-range charge ordering seen by SXPD.

3.3. ^{57}Fe Mössbauer data

At all temperatures, Mössbauer spectra of $EuBaFe_2O_5$ are dominated by components associated with valence mixing or ordering of iron atoms. Additional minor components are seen, the presence of which in the valence-mixed state corresponds to the probability of not mixing [31].

At 313 K, that is above T_p and below T_N, the ^{57}Fe Mössbauer spectrum of $EuBaFe_2O_{5.010}$ (Fig. 6) shows one dominant valence-mixed state $Fe^{2.5+}$ with its typical [25,31] six-line component and the isomer shift of ~0.6 mm/s. A more careful inspection of this sextet reveals a slight asymmetry of the absorption peaks, which was not
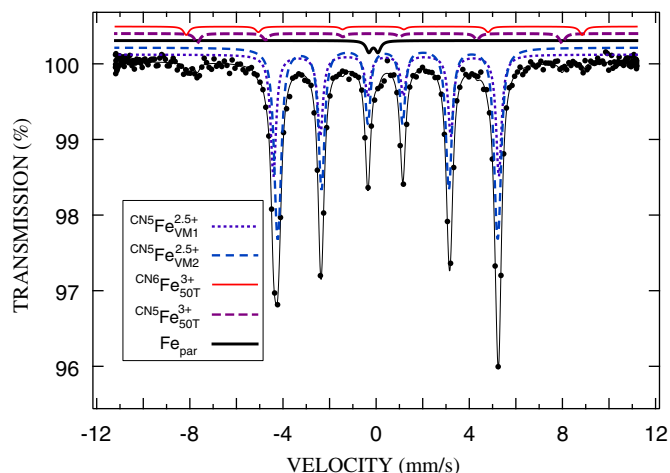
oxidized portion of the sample is being converted to the high-temperature phase first. The charge-ordered portion which survives longest upon heating has presumably its oxygen content closest to the ideal equal proportion of integer valences ($w = 0$). This would suggest that refinement data for such a charge-ordered phase (250 and 251 K) may be showing the "true" ideal long-range charge-ordered structure. In order to quantify these trends, BVS were calculated from the bond distances obtained from refinements of these isothermal scans, and are shown in Fig. 5.

Fig. 6. ^{57}Fe Mössbauer spectrum of valence-mixed EuBaFe$_2$O$_{5.010}$ at 313 K. Components used in the fitting are displayed above the data and identified in the legend.

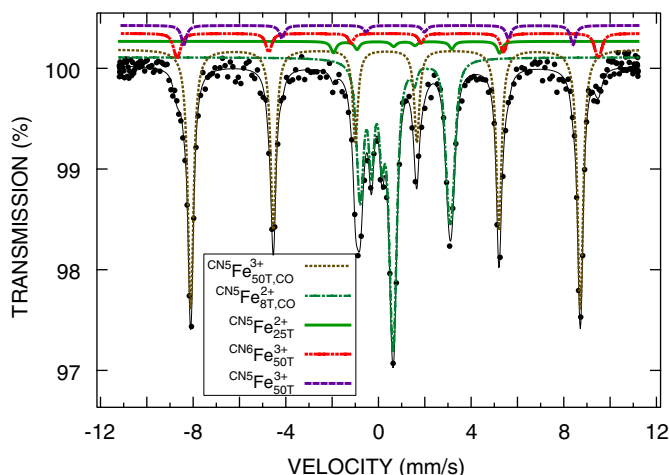Fig. 7. ^{57}Fe Mössbauer spectrum of charge-ordered EuBaFe$_2$O$_{5.010}$ at 77 K. Components used in the fitting are displayed above the data and identified in the legend.

recognized previously: the first one appears slightly broader and less deep than the sixth one. This feature can be modelled in the least-squares fits of the spectrum by using two Mössbauer components, $^{CN5}Fe_{VM1}^{2.5+}$ and $^{CN5}Fe_{VM2}^{2.5+}$, instead of one (note the oxygen coordination number indicated by the left superscript). A small difference in local coordinations around the valence-mixed iron atoms, affecting the V_{zz} values, could explain the presence of this asymmetry.

At 77 K, that is well below T_V, the typical [25,31] trivalent and divalent charge-ordered components are registered (Fig. 7): $^{CN5}Fe_{50\,T,CO}^{3+}$, where 50 T is the internal field, and $^{CN5}Fe_{8\,T,CO}^{2+}$. While the high-spin trivalent component has about half the intensity observed above T_p for the valence-mixed component, the divalent component is somewhat smaller than that. One may speculate that the local recoil-free fraction is weaker, i.e., the thermal

displacement of the Fe^{2+} atoms is larger. Such a systematic deficit in the Mössbauer absorption of the divalent iron could also explain why the average Fe valence calculated in Ref. [31] from summary of all Mössbauer components seems to slightly exceed the expected $2.5 + w$ value.

The overall Mössbauer concentration of defects in the charge-ordered phase ($^{CN5}Fe_{27\,T}^{2+}$, $^{CN5}Fe_{53\,T}^{3+}$ and $^{CN6}Fe_{50\,T}^{3+}$) is approximately 10% whereas the total entropy change from the charge-ordered state to the valence-mixed state (at T_V and T_p) is ~70% of the theoretical $2R \ln 2$ value. Also bond-valence estimates suggest that only 70% of the Fe atoms participate in the long-range charge-ordered structure. Thus, the Mössbauer data seem to give a higher degree of charge ordering. The estimate based on the Mössbauer data can be slightly lowered if the real fingerprint of the ordered state is assumed to be the $^{CN5}Fe_{8\,T,CO}^{2+}$ component (instead just subtracting the defects). Taking the concentration of ordered Fe as twice that of $^{CN5}Fe_{8\,T,CO}^{2+}$, the charge ordering at $w = 0$ is ~85%, in only slightly better agreement with the measured entropy change. The implication is that the difference is significant and is due to short-range charge ordering.

In the intermediate range between T_p and T_V, the partial separation into Fe$^{2.5-\varepsilon}$ and Fe$^{2.5+\varepsilon}$ is seen. Fig. 8 illustrates that the two main components have all the typical characteristics of being "half way" between the just described cases of charge ordering in Fig. 7 and valence-mixing in Fig. 6. The concentration of these components does not change at T_p.

The internal field of the main components is the Mössbauer parameter that exhibits the most substantial and typical variations across the two Verwey-type transitions. In Fig. 9 top, all fitted internal fields of the main Mössbauer components are plotted as a function of temperature. It is clearly seen that the change in the internal field at the premonitory charge-ordering transition, here at about 305 K, is continuous, whereas the
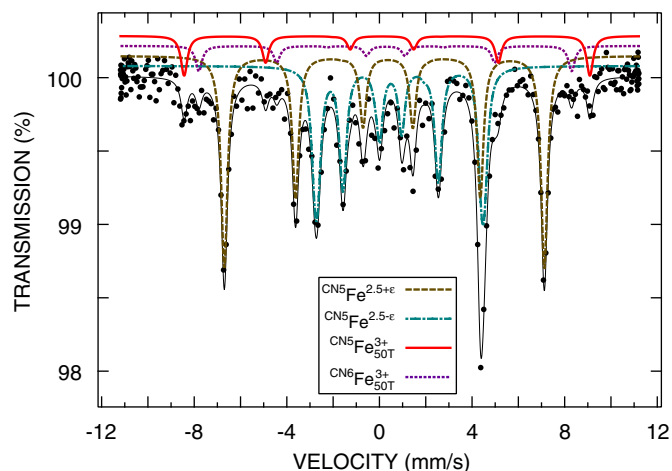

Fig. 8. ^{57}Fe Mössbauer spectrum of EuBaFe$_2$O$_{5.010}$ recorded at $T_V < 263\,K < T_p$. Components used in the fitting are displayed above the data and identified in the legend.
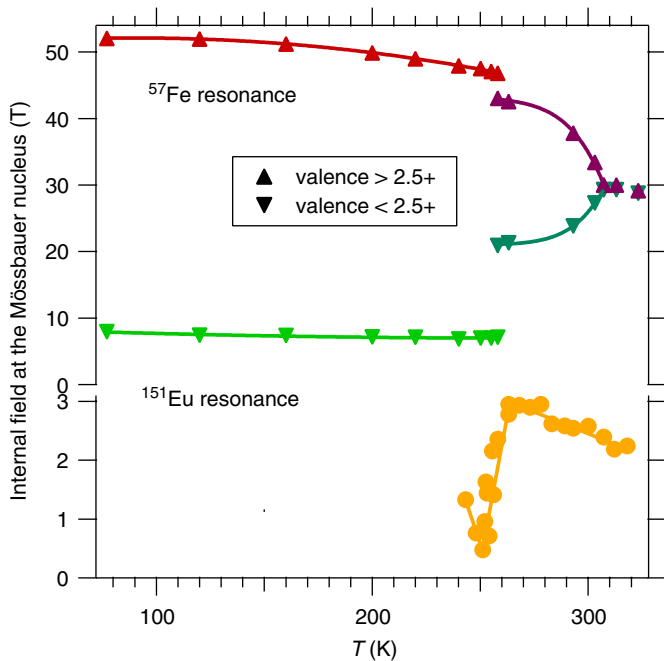
Fig. 9. Temperature dependence of internal fields refined from ^{57}Fe- and ^{151}Eu Mössbauer spectra of EuBaFe$_2$O$_{5.010}$.

change at the first-order main Verwey transition is discontinuous for both separating iron valence states.

3.4. ^{151}Eu Mössbauer data

All collected ^{151}Eu Mössbauer spectra show one broadened resonance line (Fig. 10) of trivalent Eu (Eu^{2+} would be seen around -12 mm/s). The broadening has several reasons. One of them is non-zero quadrupole coupling parameter eQ_gV_{zz}:

For valence-mixed EuBaFe$_2$O$_{5.010}$ at room temperature, a negative V_{zz} value of -3.0×10^{21} V/m^2 is obtained from fitting the spectrum. In order to verify this value, a point-charge calculation was performed, based on the actual structure parameters and iron charge 2.5+. The obtained negative V_{zz} of -0.155×10^{21} V/m^2, parallel with the c axis, stems from the flattened Eu coordination cube along c whereas an elongated unit would give positive eQ_gV_{zz}. Similarly, also EuBa$_2$Cu$_3$O$_7$ has negative V_{zz} [39]. The difference between the estimated and experimental V_{zz} value is a consequence of Sternheimer shielding [40]. The asymmetry parameter η, associated with V_{zz}, was fitted to $\sim$0.4, and is compatible with the slight orthorhombic distortion. For the charge-ordered phase, the point-charge calculations according to structure data in Table 2 also give a negative V_{zz} value of -0.159×10^{21} V/m^2, but the asymmetry parameter has increased to $\eta = 0.74$. Owing to the ordering of the iron charges, the direction of V_{zz} is no longer parallel to c, but is tilted about 60° towards a.

Above T_V, an additional broadening appears, which is asymmetric. This asymmetry only can be accounted for by introducing the internal field B as an additional fit
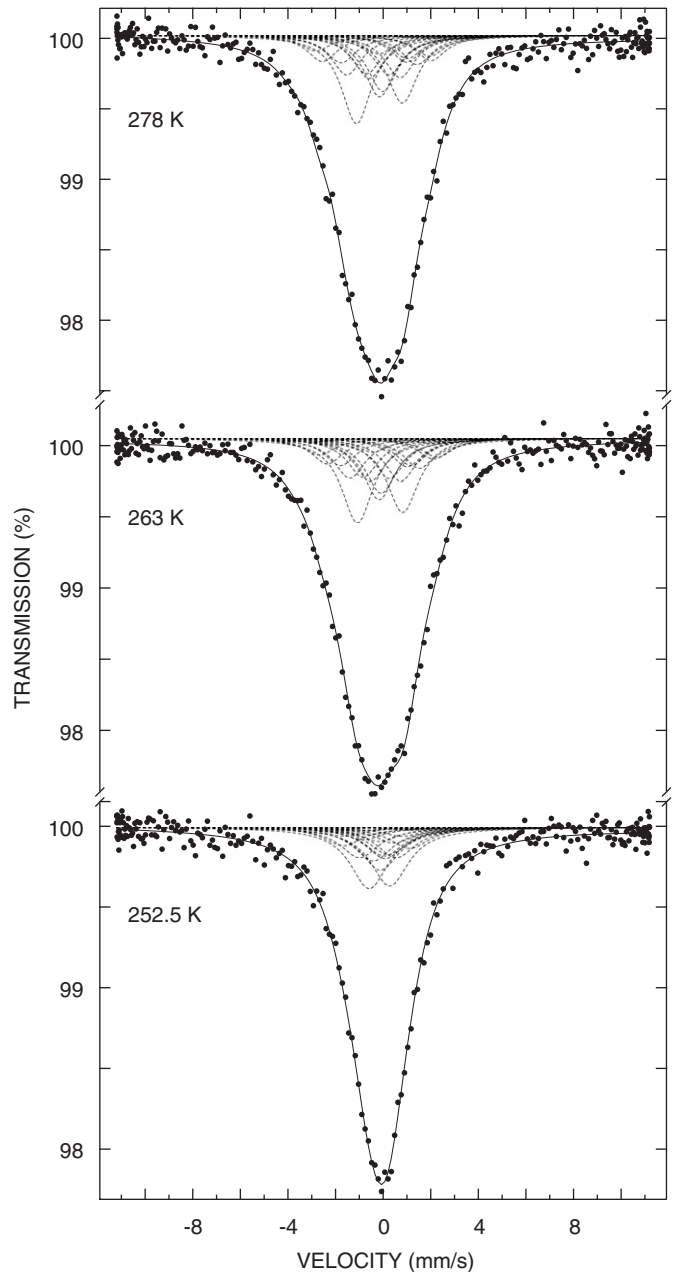

Fig. 10. ^{151}Eu Mössbauer spectra of EuBaFe$_2$O$_{5.010}$ at temperatures across the main Verwey transition.

parameter, together with the two angles α and β that link the electric-field gradient and B. For sake of consistency, ^{151}Eu spectra at all temperatures were fitted using the combined Hamiltonian, i.e., with magnetic field included. Whereas the fits improved significantly above T_V, no particular improvement was seen below this temperature.

The results show that a magnetic field of $\sim$3.0 T appears at the ^{151}Eu nucleus at the Verwey transition upon warming. Fig. 9 shows that this happens perfectly in parallel with changes in the internal field registered by the ^{57}Fe Mössbauer resonance, since these ^{151}Eu and ^{57}Fe data were obtained on the same sample loading, using the same Peltier cooling. Simultaneously, $\beta = 90°$ and α approaches

zero. In contrast, α and β are scattered below T_V because the internal field is weak (Fig. 11c).

The presence and direction of the magnetic field at the [151]Eu nucleus are both explained from the magnetic structure [25] of the title phase: whereas below T_V the field of the antiferromagnetic G-type order of iron spins cancels out at the central Eu site, above T_V the ferromagnetic coupling along the c axis across the Eu site produces a non-zero moment. Calculation with point-like magnetic moments $3.8\,\mu_B$ for valence-mixed Fe gives the Eu internal field of $\sim 0.8\,T$, parallel with the b axis. As discussed above, V_{zz} is parallel to c, and this confirms the

Fig. 11. Hyperfine parameters obtained from [151]Eu Mössbauer spectra of EuBaFe$_2$O$_{5.010}$: (a) main component of the electric field gradient, V_{zz}, (b) asymmetry parameter η, (c) angles β (squares) and α (bullets). Lines are drawn as guides for the eye.

experimental result of non-zero magnetic field perpendicular to V_{zz}.

Another interesting feature shown in Fig. 11 is that about 5 K below the just described jump in B, between 253 and 255 K, the parameters V_{zz}, η of the electric-field gradient, and the experimental line-width (not shown), exhibit a peak. The peak occurs regardless of whether or not the internal field is included in the fit. If the field is omitted for the data below 263 K, the peak becomes even clearer, as the scattering of the data points decreases. This peak occurs exactly in the middle of the first-order transition where SXPD sees two phases. It is likely that the peak is an artifact of the Mössbauer fitting of the two-phase mixture with only one single set of hyperfine parameters; on either side of the peak there is a well defined phase with well behaved hyperfine parameters. The position of this peak (Fig. 11) a few degrees below maximum in the magnetic field (Fig. 9) agrees with this conclusion as the magnetic field only occurs in the valence-mixed phase.

4. Discussion

Experimental results reported in this paper provide several sources of information on the degree of separation and ordering of iron valences across the two subsequent charge-ordering transitions in EuBaFe$_2$O$_5$. However, the methods employed will not see the same picture: X-ray diffraction registers the average atom positions in the structure as if the entire sample were ideally long-range ordered. Because the charge ordering is the last and the least perfect of the structural orders in this type structure, there are many imperfections that will decrease the degree of the charge separation as seen by SXPD. DSC detects the entropy change related to the discontinuous part of transition, and also this value is only a portion of the theoretical value of $2R\ln 2$ per formula unit for a full long-range ordering into Fe^{2+} and Fe^{3+} couples. Finally, [57]Fe Mössbauer spectroscopy accounts for all iron states, mutually ordered or disordered. The Mössbauer parameter isomer shift tells us directly about the iron valence of each of the components.

4.1. Mössbauer accounting of all states

The isomer shift of [57]Fe is sensitive to deviations of trivalent iron towards divalence. The span of the isomer shifts reported for the d^5 high-spin Fe^{3+} (0.21–0.57 mm/s) [41] is narrow, and our observed value 0.42 mm/s at 77 K for ^{CN5}Fe$^{3+}_{50\,T,CO}$ lies within it. A further support for trivalent iron is obtained from the internal field values, which were refined as high as 52.1 T. The other main component at 77 K has an isomer shift of 0.99 mm/s, and this corresponds to divalent iron (0.78–1.5 mm/s). Because the span of isomer shifts for divalent iron is rather wide, the conclusion that also this state is precisely divalent follows
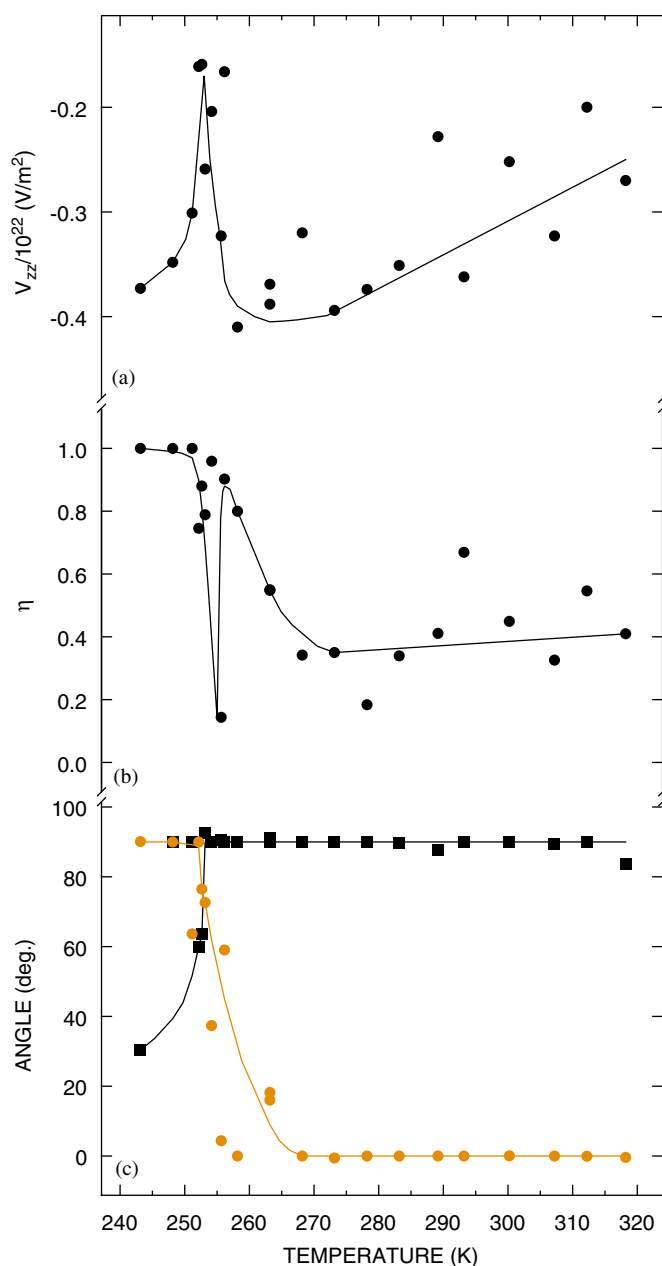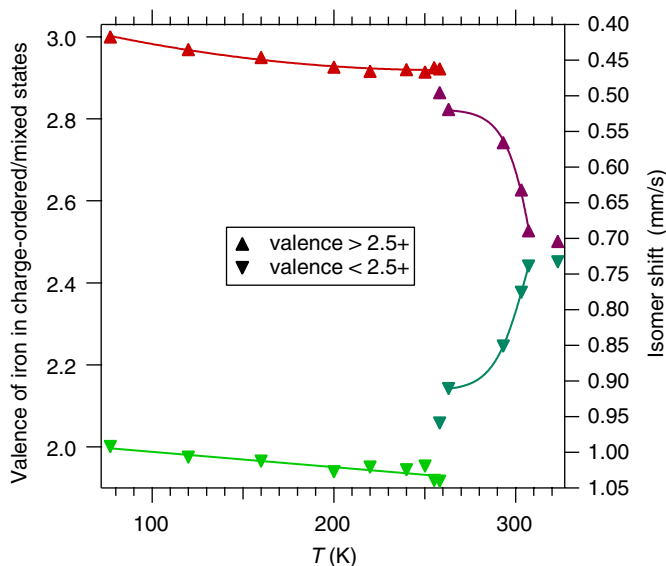
Fig. 12. Iron valences in $EuBaFe_2O_{5.010}$ derived from isomer shifts.

only indirectly from the charge-balance condition with the trivalent Fe.

The difference between isomer shifts of di- and trivalent iron allows us to estimate the iron-valence changes as a function of temperature. Fig. 12 shows results of such estimates for $EuBaFe_2O_{5.010}$. In order to be able to compare isomer shifts obtained at various temperatures, the values for all temperatures above 77 K were corrected for second-order Doppler shifts [42] by adding the difference Doppler shift between the actual temperature and 77 K; $\delta_T \approx 7 \times 10^{-4} \Delta T$ mm/s. After this correction, the isomer shift for $Fe^{2.5+}$ above T_p was exactly the average of the isomer shift values at 77 K. This means that a simple linear scale between the 77 K isomer shifts can be adopted to estimate the iron valences in the corrected isomer shift data in Fig. 12. It is seen that the iron valences separate continuously at T_p up to about 0.6 valence units just above the main charge-ordering transition. At T_V, discontinuous separation occurs to practically one full valence unit. The two Mössbauer components formed, $^{CN5}Fe^{3+}_{50\,T,CO}$ and $^{CN5}Fe^{2+}_{8\,T,CO}$, cover about 0.9 of the total Mössbauer intensity in $EuBaFe_2O_{5.010}$.

4.2. SXPD accounting of the long-range order

The bond-valence concept we use to estimate the charge-ordered valences is derived from the Pauling's 1947 formula [43] relating carbon–carbon distances and bond order via logarithmic scaling. It works equally well for polar covalent and ionic bonds. Bond-valence parameters are listed for formal charges of the cations, and these correspond to the formal valences (the number of two-electron bonds formed) within the polar covalent model. It should be kept in mind that each parameter has been obtained as an average from several structural data concerning well defined integer-valence compounds. This illustrates the point that integer valences may remain integer even if accommodated in slightly varying environments achieved under various structural compromises.

The very unequal environments of the two non-equivalent iron atoms in the charge-ordered phase at 100 K (Fig. 2) correspond to the BVS difference of 0.68 valence units (Table 3). Because the charge order is only seen as symmetry breaking displacements of O(1) and O(3) atoms, it is weaker and its extent must be less than the long-range order of Eu, Ba and the oxygen-vacancies. Two main factors decrease the long-range charge order seen by diffraction: structure defects and the powder sample inhomogeneity.

Oxygen non-stoichiometry defects interfere with the coherency of the oxygen displacements but not with the Eu, Ba ordering. In terms of the d_{xz} orbital ordering of Fe^{2+} [33], which is a Jahn–Teller effect [44], the chains of Fe^{2+} and Fe^{3+} along b are likely to break up as a coherent long-range order at defects such as twin boundaries, and oxygen defects. Of the powder sample effects, too small grains and surface imperfections would interfere with the long-range charge order, and the distribution in the oxygen non-stoichiometry across the bulk of the sample would mean that only a portion of the powder sample exhibits the maximum charge ordering, the one that has the highest T_V (Fig. 5).

In fact, Fig. 5 suggests that the long-range charge ordering in the portion of $EuBaFe_2O_{5.004}$ with highest T_V, that is the portion having most perfect stoichiometry and best long-range coherent charge order, may be approaching one valence unit. This would be in agreement with the Mössbauer data discussed in the previous paragraph and would mean that the BVS charge-ordering fraction of 0.68 actually represents the degree of the long-range ordering of practically integer valences. Although the diffraction data per se do not prove that the ordered valences must be integers, Fig. 12 shows how an only *partial* valence separation looks like: its magnitude according to the Mössbauer isomer shift may be as large as 0.5 valence units, but it can still be accommodated with no structural consequences seen by powder diffraction.

5. Conclusions

^{57}Fe Mössbauer spectroscopy identifies one of the two charge-ordered states in $EuBaFe_2O_5$ as trivalent. This implies that the second state is divalent. High-intensity, high-resolution SXPD patterns of $EuBaFe_2O_{5.004}$ can be refined into full structural data also in the two-phase system across the Verwey transition. The result shows that the long-range ordered charge separation between the iron atoms approaches one valence unit in the most stoichiometric (defect-free) portion of the sample, right before the ordered phase disappears upon further heating. In contrast, typical partial separation of iron charges, which actually occurs in this phase between T_V and T_p, corresponds to about 0.5 valence units, as evaluated from ^{57}Fe Mössbauer isomer shifts.

In the $EuBaFe_2O_{5.004}$ sample of low and fairly homogeneous oxygen non-stoichiometry, the average charge separation derived from powder diffraction data is 0.68 valence units (at 100 K). Rather than all iron atoms being present in two valences separated by 0.68, this needs to be interpreted as 68% of iron atoms in the powder sample being ordered into a long-range pattern of integer valences. This is because also the total transition entropy per formula is about 0.7 of the $2R \ln 2$ value (per formula unit) valid for *all* iron atoms being *fully* charge ordered. Neither the ^{57}Fe Mössbauer spectroscopy provides any support for 100% iron atoms being charge ordered, as it registers their total fraction of about 0.9. Because the resolution of the Mössbauer spectroscopy is not limited to the long-range order, the difference is attributed to a short-range charge order of about 20% of iron atoms in a powder sample of $EuBaFe_2O_5$ below the Verwey-type transition.

While the ^{151}Eu Mössbauer spectroscopy, as a probe into the local environment of the Eu atom in $EuBaFe_2O_5$, does not register quantitative data for the charge ordering below Verwey transition, it offers a selective view into the ferromagnetic coupling of the valence-mixing iron pairs across the Eu layer along c above the Verwey transition. This is because the field of the G-type ordered iron moments below the Verwey transition cancels out at the Eu nucleus whereas it does not for the magnetic order above the transition.

Acknowledgments

References

[1] E.J.W. Verwey, Nature (London) 144 (1939) 327–328.
[2] J.P. Wright, J.P. Attfield, P.G. Radaelli, Phys. Rev. Lett. 87 (2001) 266401/1–266401/4.
[3] R.J. Goff, J.P. Wright, J.P. Attfield, P.G. Radaelli, J. Phys. Condens. Matter 17 (2005) 7633–7642.
[4] E. Nazarenko, J.E. Lorenzo, Y. Joly, J.L. Hodeau, D. Mannix, C. Marin, Phys. Rev. Lett. 97 (2006) 056403/1–056403/4.
[5] H.-T. Jeng, G.Y. Guo, D.J. Huang, Phys. Rev. Lett. 93 (2004) 156403/1–156403/4.
[6] H. Uzu, A. Tanaka, J. Phys. Soc. Jpn 75 (2006) 043704/1–043704/4.
[7] M.P. Pasternak, W.M. Xu, G.Kh. Rozenberg, R.D. Taylor, R. Jeanloz, J. Phys. Chem. Solids 65 (2004) 1531–1535.
[8] G.Kh. Rozenberg, M.P. Pasternak, W.M. Xu, Y. Amiel, M. Hanfland, M. Amboage, R.D. Taylor, R. Jeanloz, Phys. Rev. Lett. 96 (2006) 045705/1–045705/4.
[9] G. Subías, J. García, J. Blasco, Phys. Rev. B 71 (2005) 155103/1–155103/9.
[10] P. Novák, H. Štěpánková, J. Englich, J. Kohout, V.A.M. Brabers, Phys. Rev. B 61 (2000) 1256–1260.
[11] D. Schrupp, M. Sing, M. Tsunekawa, H. Fujiwara, S. Kasai, A. Sekiyama, S. Suga, T. Muro, V.A.M. Brabers, R. Claessen, Europhys. Lett. 70 (2005) 789–795.
[12] F.J. Berry, S. Skinner, M.F. Thomas, J. Phys. Condens. Matter 10 (1998) 215–220.
[13] J. García, G. Subías, J. Phys. Condens. Matter 16 (2004) R145–R178.
[14] G. Subías, J. García, J. Blasco, M.G. Proietti, H. Renevier, M.C. Sánchez, Phys. Rev. Lett. 93 (2004) 156408/1–156408/4.
[15] J. García, J. Blasco, M.C. Sánchez, M.G. Proietti, G. Subías, Surf. Rev. Lett. 9 (2002) 821–830.
[16] J.P. Shepherd, R. Aragon, J. Koenitzer, J.M. Honig, Phys. Rev. B 32 (1985) 1818–1819.
[17] J.M. Honig, J. Alloys Comp. 229 (1995) 24–39.
[18] K. Siratori, N. Mori, H. Takahashi, G. Oomi, J. Iida, M. Tanaka, M. Kishi, Y. Nakagawa, N. Kimizuka, J. Phys. Soc. Jpn 59 (1990) 631–636.
[19] Y. Shimakawa, T. Numata, J. Tabuchi, J. Solid State Chem. 131 (1997) 138–143.
[20] D. Ihle, B. Lorenz, Phys. Status Solidi B 116 (1983) 539–546.
[21] V. Ksenofontov, H.C. Kandpal, J. Ensling, M. Waldeck, D. Johrendt, A. Mewis, P. Guetlich, C. Felser, Europhys. Lett. 74 (2006) 672–678.
[22] P. Karen, P.M. Woodward, J. Mater. Chem. 9 (1999) 789–797.
[23] P. Karen, P.M. Woodward, P.N. Santosh, T. Vogt, P.W. Stephens, S. Pagola, J. Solid State Chem. 167 (2002) 480–493.
[24] J. Lindén, P. Karen, J. Nakamura, M. Karppinen, H. Yamauchi, Phys. Rev. B 73 (2006) 064415/1–064415/7.
[25] P. Karen, P.M. Woodward, J. Lindén, T. Vogt, A. Studer, P. Fisher, Phys. Rev. B 64 (2001) 214405/1–214405/14.
[26] P. Karen, J. Solid State Chem. 177 (2004) 281–292.
[27] Z. Kąkol, J. Solid State Chem. 88 (1990) 104–114.
[28] J.P. Wright, A.M.T. Bell, J.P. Attfield, Solid State Sci. 2 (2000) 747–753.
[29] J.P. Wright, J.P. Attfield, P.G. Radaelli, Phys. Rev. B 66 (2002) 214422/1–214422/15.
[30] E. Goering, S. Gold, M. Lafkioti, G. Schütz, V.A.M. Brabers, Phys. Rev. Lett. 72 (2005) 033112/1–033112/4.
[31] J. Lindén, P. Karen, A. Kjekshus, J. Miettinen, T. Pietari, M. Karppinen, Phys. Rev. B 60 (1999) 15251–15260.
[32] P. Karen, J. Solid State Chem. 170 (2003) 9–23.
[33] P.M. Woodward, P. Karen, Inorg. Chem. 42 (2003) 1121–1129.
[34] P.M. Woodward, E. Suard, P. Karen, J. Am. Chem. Soc. 125 (2003) 8889–8899.
[35] J.P. Attfield, Solid State Sci. 8 (2006) 861–867.
[36] A.C. Larson, R.B. Von Dreele, General Structure Analysis System (GSAS), Los Alamos National Laboratory Report LAUR 86-748, 2000.
[37] P.W. Stephens, J. Appl. Cryst. 32 (1999) 281–289.
[38] I.D. Brown, The Chemical Bond in Inorganic Chemistry, in: The Bond Valence Model, Oxford University Press, Oxford, 2002, pp. 225–226.
[39] Z.M. Stadnik, G. Stroink, R.A. Dunlap, Phys. Rev. B 39 (1989) 9108–9112.
[40] P. Gütlich, in: U. Gonser (Ed.), Topics in Applied Physics V, Mössbauer Spectroscopy I, Springer, Berlin, 1975, p. 61.
[41] N.N. Greenwod, T.C. Gibb, Mössbauer Spectroscopy, Chapman & Hall, London, 1971, p. 91.
[42] P. Gütlich, in: U. Gonser (Ed.), Topics in Applied Physics V, Mössbauer Spectroscopy I, Springer, Berlin, 1975, p. 33.
[43] L. Pauling, J. Am. Chem. Soc. 69 (1947) 542–553.
[44] J.B. Goodenough, Phys. Rev. 100 (1955) 564–573.